Post-Print of an Accepted Manuscript on the Laboratory of Turbulent Flows Website

The Accepted Manuscript begins on the next page.

Effect of Disk Angle-of-Attack on Aerodynamic Performance of Small Propellers

David Serrano, Max Ren, Ahmed Jawad Qureshi, Sina Ghaemi*

Department of Mechanical Engineering, University of Alberta, Edmonton, Alberta, Canada,

*ghaemi@ualberta.ca

The aerodynamic performance of four 12-inch diameter propellers was investigated at propeller disk angles-of-attack ranging from 0° to 90° and at advance ratios ranging from 0 to 0.55. Aerodynamic load measurements using a six-axis load cell showed that the thrust of all four propellers increased with an increasing disk angle-of-attack, for all the advance ratios investigated. On the other hand, power consumption demonstrated lower sensitivity to variations in the propeller angle-of-attack. The load difference between the advancing and retreating blades caused pitch and yaw moments, which increased with an increasing propeller angle-of-attack. When plotted as a function of the inflow advance ratio, the thrust, power and propulsive efficiency plots overlapped for the range of disk angle-of-attacks. Analytical prediction of the performance of the rotor was carried out using blade element theory. Comparisons of the experimental data acquired and the predictions using different inflow models was made. The evaluation showed that the Glauert [15] and Coleman *et al.* [16] inflow models are capable of predicting propeller performance at a wide range of non-zero disk angle-of-attack with maximum discrepancy of 15%.

Keywords: Propeller at an angle of attack, Unmanned Aerial vehicle, Wind tunnel testing

Nomenclature

A = area of the rotor disk, in meters squared.

a_1, a_2, a_3 and a_4 = parameters of the correction factors f_1 and f_2.

C_P = coefficient of power.

C_T = coefficient of thrust.

$C_{T,h}$ = coefficient of thrust for the hover condition (zero free-stream).

c	=	chord of an elemental blade section, in millimeters.
D	=	nominal diameter of the propeller, in millimeters.
d	=	separation distance between the rotor hub and the center of the load cell, in millimeters.
dT	=	differential thrust, in Newtons.
F_x	=	x-component of force measured by the load cell, in Newtons.
F_y	=	y-component of force measured by the load cell, in Newtons.
F_z	=	z-component of force measured by the load cell, in Newtons.
f_1, f_2	=	linear correction factors applied in the induced velocity models.
J	=	advance ratio based on the free stream velocity.
J_a	=	inflow advance ratio, based on the free-stream component perpendicular to the propeller disk.
J_a'	=	non-dimensional inflow advance ratio
J_t	=	tangential advance ratio, based on the free-stream component tangent to the propeller disk.
k_x, k_y	=	longitudinal and lateral weighting factors in the linear inflow model, respectively.
M_x	=	x-component of moment with respect to the load-cell center, in Newton-meters.
M_y	=	y-component of the moment generated by the propeller with respect to the load-cell center, in Newton-meters.
M_z	=	z-component of moment with respect to the load-cell center, in Newton-meters.
$M_{y,LC}$	=	y-component of total moment with respect to the load-cell center, in Newton-meters.
n	=	propeller's rotation velocity, in revolutions-per-second.
N	=	number of blades.
P	=	power consumed by the propeller, in Watts.
r	=	radial coordinate, originating at the center of the rotor disk.
R	=	radius of the propeller disk, in meters.
R_{eff}	=	effective blade radius.
V_a	=	component of the relative wind perpendicular to the rotor disk, in meters-per-second.
V_∞	=	free stream velocity, in meters-per-second.
V_R	=	resultant relative wind vector, incident on the blade element, in meters-per-second.
V_t	=	component of the relative wind that is tangent to the rotor plane, in meters-per-second.

v_h = induced velocity in hover (zero free-stream), in meters per second.

v_i = induced velocity, in meters per second.

x, y, z = Cartesian coordinates of the propeller's coordinate system.

α_P = angle-of-attack of the propeller disk with respect to the free stream, in degrees.

α_b = effective angle-of-attack of a blade element, in degrees.

$\alpha_{L=0}$ = zero lift angle-of-attack of the cross-sectional airfoil, in degrees.

η = propulsive efficiency

χ = wake skew angle, in degrees.

λ = inflow ratio.

λ_i = induced inflow ratio, calculated using linear inflow model.

λ_h = induced inflow ratio in the hover condition, from momentum theory.

λ_0 = induced inflow ratio in axial flight, from momentum theory.

μ = dynamic viscosity of air, in kilograms per meter second.

Ω = angular velocity of the propeller, in radians-per-second.

φ = inflow angle, in degrees.

ψ = azimuthal angle in the circumference of the rotor disk, in degrees.

θ = pitch angle of the blade section, in degrees.

1   Introduction

The majority of small unmanned aerial vehicles (UAVs) implement a multi-rotor configuration to carry out maneuvers such as hovering and vertical take-off and landing. While the multi-rotor propulsion simplifies the control system and increases the maneuverability of the vehicle, it is not as efficient as a fixed-wing vehicle for forward flight, an inefficiency that limits the range and endurance of small multi-rotor UAVs.

The forward flight of a multi-rotor vehicle is typically achieved by tilting the rotor disk (and the vehicle) to project a component of the propeller thrust in the direction of motion. Therefore, the rotor will operate with its disk at a non-zero angle-of-attack, α_P, with respect to the free-stream velocity. The projection of the free-stream velocity perpendicular and parallel to the rotor disk results in variation of the effective angle-of-attack, α_b, and the generated force of the blade elements. As a result, the aerodynamic performance of the rotor deviates from that of a conventional

3

propeller with the rotor disk perpendicular to the free-stream. In extreme conditions, the variation of α_b can also cause local flow separation over the propeller disk and reduce net thrust. The load non-uniformity over the propeller disk can also result in yaw, pitch or rolling moments on the vehicle, affecting its stability. An understanding of the aerodynamic performance of small propellers at a wide range of disk angles is required for analysis of UAVs' design and flight performance. This requirement is different from that of helicopters and propeller-powered airplanes, which operate in an approximate α_P range of $80° \leq \alpha_P \leq 90°$ and $0° \leq \alpha_P \leq 10°$, respectively. A multi-rotor UAV performs a variety of maneuvers in a single flight mission, which requires rotor operation at a wide range of angles-of-attack covering $0° < \alpha_P < 90°$.

Previously, the majority of the experiments for small UAV propellers operating in $50,000 < Re < 100,000$ (based on the chord length, c, of propeller blade elements) have been developed for axial flow condition with $\alpha_P = 0°$. Brandt and Selig [1] measured the performance of 79 propellers from a variety of manufacturers (e.g., APC, Master Airscrew, Graupner, and GWS), ranging in diameter from 9 to 11 inches in axial flow condition. The tests were conducted at a fixed rotational speed of 1,500 and 7,500 revolutions per minute (RPM) and a maximum free-stream velocity of 24.38 m/s. They observed a maximum efficiency of 65%, and improved system performance with an increase in the rotational speed of the propeller. The extensive database developed by Brandt and Selig [1] provides UAV designers with readily available data for zero α_P. However, it does not include any experiment on propellers operating at non-zero α_P for modern multi-rotor vehicles.

There have been a number of investigations of large propellers at non-zero α_P for large, vertical takeoff and landing (VTOL) aircrafts. Kuhn and Draper [2] tested the performance of multiple propellers and a wing-propeller combination for a VTOL vehicle in a range of $0° < \alpha_P < 90°$. The propellers used by Kuhn and Draper [2] were 2 feet in diameter, had three blades, a Clark Y cross-sectional airfoil, and operated at collective angles of 8° and 20°. A maximum propulsive efficiency of ~77% was achieved at collective angle of 20°. By adjusting the rotational speed of the propeller, the experiments were carried out at constant thrust, which showed an increase of C_T (normalized by RPM) with increase of α_P. McLemore and Cannon [3] investigated the aerodynamic performance of a two-propeller tandem system in the $0° < \alpha_P < 180°$ range. The propellers were 5.33 feet in diameter, two-bladed, and the collective blade angle was varied from 0° to 67.5°. They presented their results as a function of two different advance ratios. First, the free-stream advance ratio, defined as

$$J = \frac{V_\infty}{nD},$$ (1)

where V_∞ is the free-stream velocity, n is the angular velocity of the propeller, and D is the nominal diameter of the propeller. And second, the inflow advance ratio, which is defined based on the component of the free-stream velocity that is perpendicular to the rotor disk, defined as

$$J_a = \frac{V_\infty \cos(\alpha_P)}{nD},$$ (2)

and varied within $0 < J_a < 6.2$. Their results demonstrated that thrust and power coefficients increase with an increase of α_P at a given J_a as long as there is no flow separation over the blades. McLemore and Cannon [3] also showed that the J_a value that corresponds to $C_T = 0$ increased with increase of α_P. To investigate their operation for a VTOL aircraft, Yaggy and Rogallo [4] performed wind tunnel experiments on three different propellers operating within $0° < \alpha_P < 85°$. Propeller blades with NACA 16-series, NACA 64-series and a NACA 0009 airfoils and rotor diameter of 12, 10, and 9.5 feet were investigated, respectively. They observed that increasing α_P resulted in an increase of the rate of change of C_T, C_P, C_{Fx}, C_{Mx} and C_{My} with a variation of J_a.

There are a limited number of investigations available regarding the performance of small propellers for multi-rotor UAVs operating at non-zero α_P. Hughes and Gazzaniga [5] evaluated the effect of α_P ranging from -16° to 16° on two counter-rotating propellers (~21 to 24 inch in diameter), arranged in a tandem (coaxial) configuration, to simulate takeoff and landing flight regimes. They concluded that, within the relatively small range of -16° to 16°, there was no variation in the efficiency and power coefficient with respect to α_P. Hughes and Gazzaniga [5] highlighted that η and C_P for different α_P collapse when presented as a function of the inflow advance ratio (J_a). More recently, Pereira [6] investigated a rotor with 16 cm diameter for $0 \leq J_a \leq 0.4$ and $0° \leq \alpha_P \leq 90°$. They observed that, for increasing J_a and α_P, the thrust generated, as well as the power consumed by the propeller, increased. In a recent investigation, Carrol [7] tested a two-bladed propeller (T-Motor) with 18 inch diameter, 6.1 in/rev pitch, at α_P range of $-30° \leq \alpha_P \leq 90°$, up to a maximum J value of ~0.35. The tests were performed at three rotating speeds of 3,000, 4,000, and 5,000 RPM. They demonstrated that for increasing α_P and increasing J values, the thrust generation of the propeller increased. However, the power consumption at $\alpha_P < 30°$ increased with an increase of α_P and an increase of J, while for $\alpha_P \geq 30°$, the power consumption reduces with a parabolic trend.

Carrol [7] developed and evaluated an analytical model to predict the performance of a propeller both when it is isolated and when it is in the presence of neighboring rotors. The analytical model was based on blade element theory

(BET), where axial and edgewise flow a uniform λ was applied for hover. For small angle forward flight a radial distribution of λ was used, and for large forward flight angles a wake-interaction model based on vortex theory was used to determine the distribution of λ over the rotor disk. However, most current design tools for the analysis of propellers (e.g., Drela [8]), based on blade element theory, are still limited to $\alpha_p = 0°$, including the approximations for tip losses (e.g. Goldstein [9]). In a combined experimental and numerical investigation, Theys et al. [10] evaluated the performance of BET and vortex lattice method (VLM) to predict propeller performance at a wide range of disk angle-of-attack. The comparison showed that both BET and VLM methods fail to predict propeller performance at large α_P. They proposed a correction factor based on the wake skew angle to improve the performance predictions for the tested propellers and flight conditions.

The purpose of this study is to investigate the aerodynamic performance of propellers designed for small UAVs in operating conditions with non-zero α_P. Two propeller models, namely the Slow Flyer and Sport models from APC Propellers, with nominal diameter of 12 inches are tested in a range of $0° \leq \alpha_P \leq 90°$ and a free-stream advance ratio range of $0 \leq J \leq 0.55$. Measurements of thrust, power, moments and propulsive efficiency are provided. In addition to the experimental work, the propeller performance is investigated using the blade element theory for $0° \leq \alpha_P \leq 90°$ with different models for estimating the induced velocity. The performance of the existing induced velocity models are compared with the experimental data. The results provide a database for UAV design and enhance the understanding of propeller operation at non-zero α_P.

2 Experimental Setup

2.1 Wind tunnel

The experiments were performed in the closed-loop wind tunnel facility at the University of Alberta. The test section has a rectangular cross-section of 1.2 m height and 2.4 m width, which follows a contraction section with area ratio of 6.3:1. The maximum achievable flow velocity at the test section is approximately 30 m/s. However, the tests were only conducted up to a maximum wind speed of 20 m/s, relevant to small-scale UAVs. The wind tunnel is equipped with a Pitot tube and a thermocouple to obtain instantaneous speed and temperature measurements in the test section. The maximum turbulent intensity at the test section has been measured to be less than 0.4%.

2.2 Propeller system

Two propeller models, commercially known as the Slow Flyer (SF) and Sport (SP) models from APC Propellers, were used in the investigations. The two models have several geometrical differences, mainly in the airfoil geometry, and the chord distribution along the blade. The exact airfoil geometries of the propellers are proprietary information of APC Propellers. However, as per information provided by the manufacturer, the SF model may be approximated using an Eppler 63 airfoil, and the SP model using a NACA 4412 airfoil, as shown in Fig. 1 (a) and (b), respectively. These two airfoils have stall angle-of-attack of $\alpha_b=9°$ and $\alpha_b=14°$, and zero-lift angle-of-attack of $\alpha_{L=0}=-2°$ and $\alpha_{L=0} = -4°$, respectively.

(a)   (b)
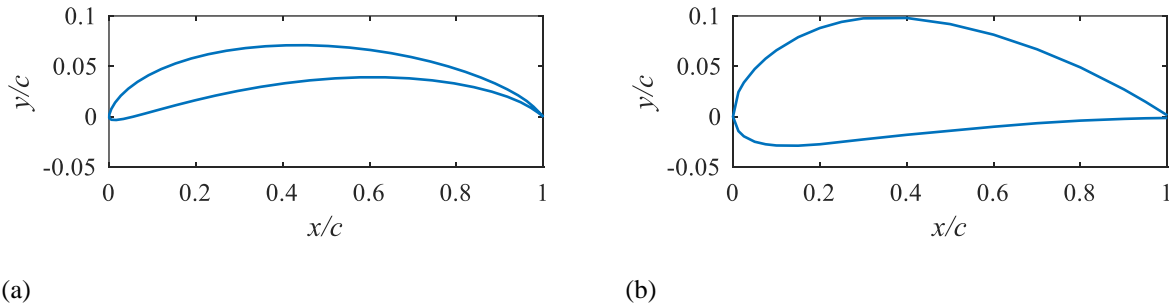
Fig. 1 The cross section of the SF and the SP propellers resembles an (a) Eppler 63 airfoil, and (b) a NACA 4412 airfoil, respectively, obtained from [11]

Two SF propeller blades with 4.7 and 6 inch/rev pitch and two SP propellers with 5 and 6 inch/rev pitch were used. All four propellers tested had a diameter of 12 inches and two blades. The nomenclature used to identify each propeller in this work, consists of an abbreviation of the propeller model, followed by the nominal diameter, multiplication sign, and the nominal pitch. For example, the SF model with 12 in diameter and 6 inches/revolution

would be SF12×6. The distributions of pitch angle and the chord length of the propeller blades in the radial direction were estimated by imaging the blade on two orthogonal planes. The pitch angle distribution is shown in Fig. 2(a), while the chord length variation is shown in Fig. 2(b). The curves in Fig. **2** (a) and (b) were obtained using 60 discrete measurement points along the radial direction of the blade and fitted with a fourth order polynomial.

A brushless DC (BLDC) outrunner (external casing rotation) motor with 1,000 K_V and 75 Hz electronic speed controller (ESC) (Phoenix Edge) were used in all the experiments. The motor is capable of rotating at a maximum unloaded (no blade rotation or free stream) angular speed of 12,000 RPM using a 12 V power supply. The maximum allowable rotation of the SF and SP propellers is 5,400 RPM and 15,800 RPM, respectively. Choosing a small speed of 5,000 was not desirable for the SP since this propeller would windmill at high freestream velocities (i.e. large J). In addition, for a large rotational speed, experiments at a large J require a large free-stream velocity, which may not be feasible. For example, a free stream velocity of 41.91 m/s is required for $J = 0.55$ if a rotational speed of 15,000 RPM was chosen. Therefore, to achieve the same range of advance ratios for SF and SP propellers, the angular speed was maintained at a constant value of 5,000 RPM for the SF model, and 8,000 RPM for the SP model.

(a)   (b)
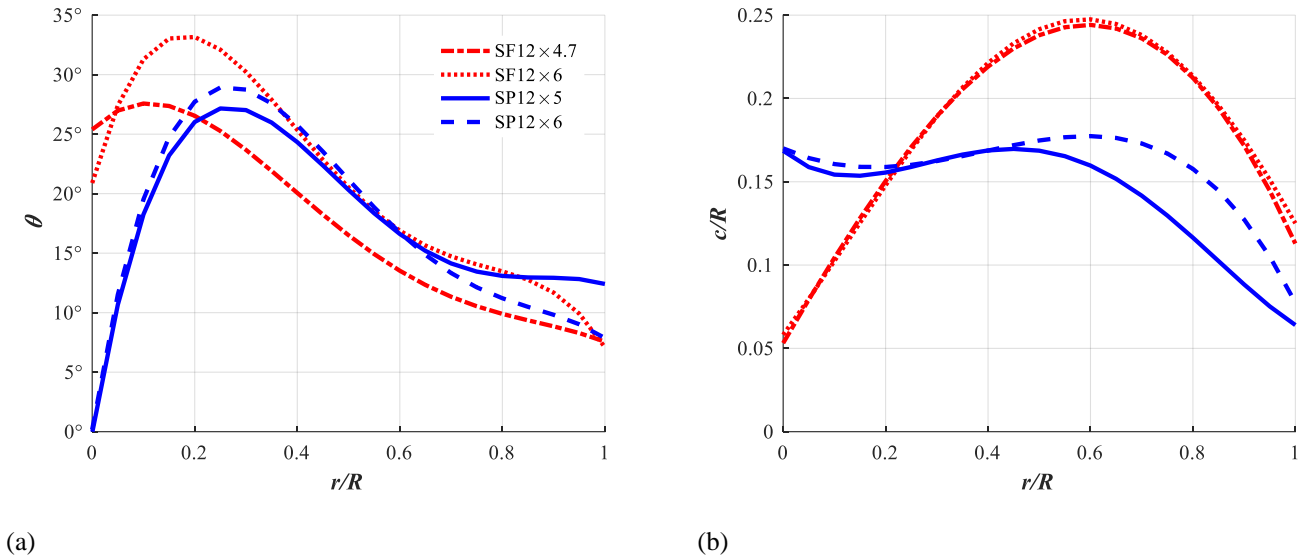
Fig. 2 (a) The pitch angle distribution, and (b) chord length distribution of the four tested propellers estimated by projection of the blade shape on two orthogonal planes.

2.3 Six-axis load cell

Aerodynamic forces and moments acting on the *x*, *y* and *z* directions as defined by the coordinate system of Fig. 3(a) is obtained using a six-axis force/torque transducer (Mini45, ATI Industrial Automation). This load cell is capable of measuring the three force components, F_x, F_y, and F_z (thrust), as well as the three components of moments M_x, M_y, and M_z, which are also shown in Fig. 3(c). The transducer is capable of measuring forces in the range of ±145 N for the F_x and F_y components, ±290 N for the F_z component, and ±5 Nm for all the moments. The coordinate system of the load cell is specified with x_{LC}, y_{LC} and z_{LC} in Fig. 3(c) and has the same orientation as the coordinate system of the propeller. The origin of the load-cell coordinate system is located at *x*=0, *y*=0 and *z*=-108 mm with respect to the propeller coordinate system.

The blade rotating against the free-stream is called the 'advancing' blade, and the blade rotating in the direction of the free stream is indicated as the 'retreating' blade for a propeller operating at a non-zero value of α_P, as specified by the shaded areas in Fig. 3(c). As a result of variation in the incident velocity vector at the leading edge of the blade, the advancing and retreating blades operate at different effective angle-of-attack α_b. The force imbalance between the advancing and retreating blades also results in a moment about the *y*-axis of the propeller. To obtain the moment about the *y*-axis of the rotor hub, M_y, the moment of the side force, F_x, measured at the load-cell has to be considered. Therefore, M_y is calculated by subtracting the total moment measured by the load cell, $M_{y,LC}$, and the *y*-moment generated by the force, F_x, acting upon the moment arm *d* (=108 mm) as:

$$M_y = M_{y,LC} - F_x \cdot d. \tag{3}$$

Since the propeller's hub and motor are concentric with the load cell, the forces F_x and F_y do not contribute to the moment, M_z. Therefore, the torque required to rotate the propeller is equal to the moment, M_z, and the required power, *P*, is obtained as:

$$P = M_z \cdot \Omega, \tag{4}$$

where Ω is the angular velocity in rad/s.

2.4 Mounting system

The propeller, motor and load cell are connected to a custom made stinger supported by a vertical shaft, as shown in Fig. 3. The stinger support was designed and manufactured to have minimal interference on the upstream flow. The support is mounted on a vertical shaft, which is connected to a rotary turntable located below the test section. The turntable is manually operated, and allows the stinger support to be rotated 360° about the longitudinal axis of the

9

vertical shaft, in increments of 0.5°. The angle-of-attack, α_P, is defined as the angle generated between the z-axis of the load cell coordinate system and the free stream velocity, as represented in Fig. 3(b). In this experiment, $\alpha_P = 0°$ represents axial flow with free stream perpendicular to the rotor disk. The $\alpha_P = 90°$ represents the complete edgewise flow when the free-stream is parallel to the rotor disk.

(a)

(b)
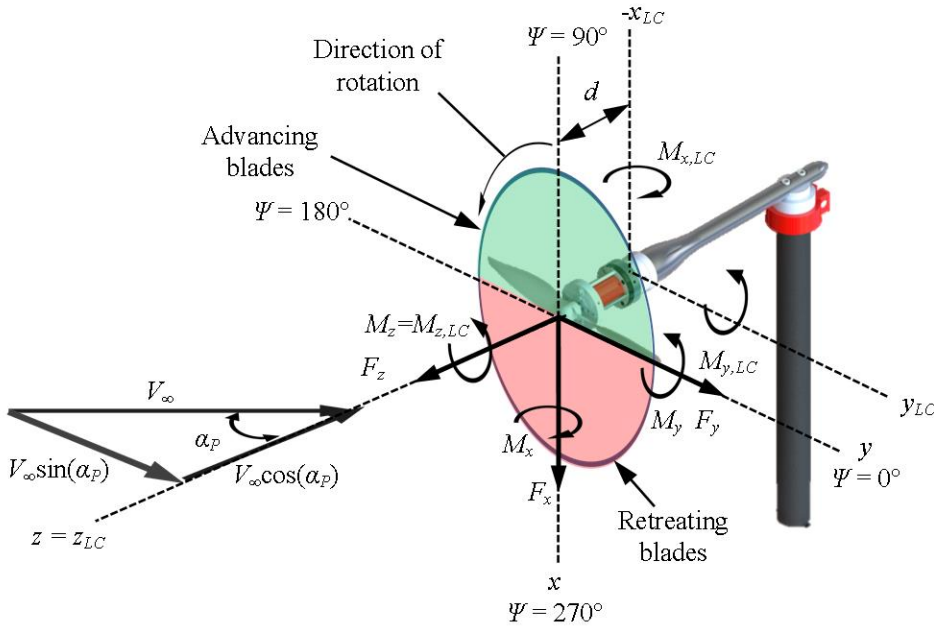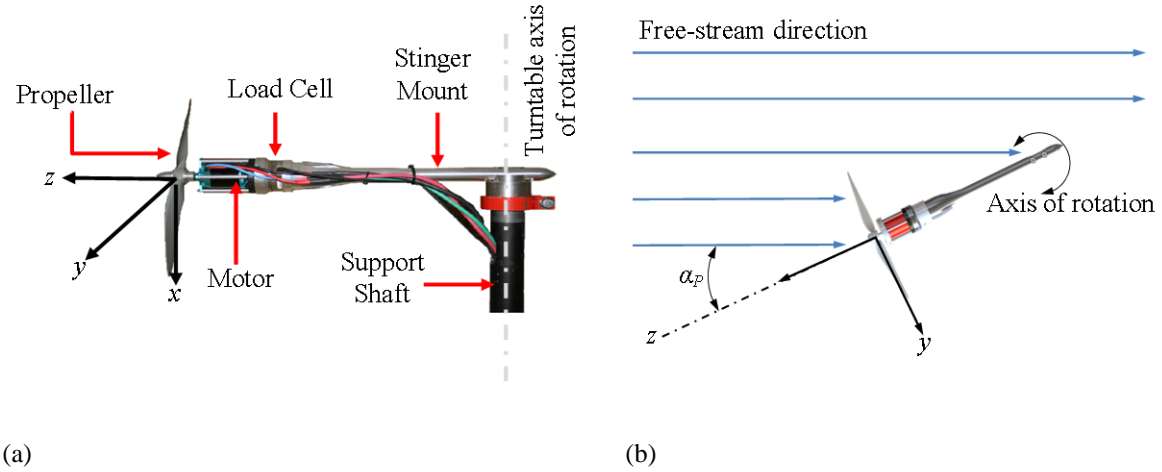
(c)

Fig. 3 A schematic view of the experimental setup showing the main components and the coordinate systems. (a) side view, (b) top view also showing the definition of the rotor disk angle-of-attack α_P, (c) isometric view showing the relevant forces and moments, the free stream velocity vector and its projections.

2.5 Data acquisition

The output voltage of the load cell was recorded using a data acquisition (DAQ) card (NI USB-6218, National Instruments) with 16 bit resolution. The load cell data was collected at a frequency of 100 Hz for a duration of 60 sec for each test condition. The ESC was programmed to output the angular speed of the motor in revolutions-per-minute, which was recorded at a frequency of 10 Hz. The data logging and the control of the BLDC motor using a pulse width modulation (PWM) signal control were also performed using the NI USB-6218 DAQ card with LabVIEW (National Instruments) interface. For every round of data acquisition, the load cell offset due to the drag of the motor body was removed before turning on the propeller. The experimental condition of the investigations is summarized in Table 1. The free-stream velocity was varied in increments of 2 m/s, from zero to 14 m/s for the SF models, and from zero to 20 m/s for the SP propellers. The angle-of-attack of the propeller disk was varied in increments of 10° from $\alpha_P = 0°$ to 90° for each velocity, expect for $V_\infty = 0$ m/s in which the value of α_P is irrelevant to the performance of the propeller.

Table 1: Summarized test matrix of the investigation.

Propeller Model	Propeller pitch, inch/rev	n, RPM	V_∞, m/s with steps of 2 m/s	J	α_P with steps of 10°
Slow Flyer (SF)	4.7, 6	5,000	0 – 14	0 – 0.55	0° – 90°
Sport (SP)	5, 6	8,000	0 – 20	0 – 0.5	0° – 90°

2.6 Data Reduction

The rotor performance is evaluated by its propulsive efficiency, η, which depends on thrust, power consumption, and the advance ratio, as described by the following expression:

$$\eta = \frac{C_T J}{C_P} \cdot 100,$$

(5)

where C_T is the non-dimensional coefficient of thrust defined by Glauert [12] as:

$$C_T = \frac{F_z}{\rho n^2 D^4},$$

(6)

and C_P is the non-dimensional coefficient of power, which using equation (4) for the propeller power, can be expressed as,

$$C_P = \frac{M_z \Omega}{\rho n^3 D^5}.$$

(7)

11

In equations (6) and (7) the symbol ρ denotes the density of air. The density values used in the computation of these coefficients were obtained based on the average temperature recorded during each test. To evaluate the effect of changing the free-stream and the net inflow into the rotor disk on the performance of the propeller in the results section of this paper, the thrust, power and efficiency data are presented as functions of both J and J_a, respectively. In this investigation, the units for n in equation (1) will be revolutions-per-seconds. Where the efficiency is presented as a function of J_a, it is represented by the symbol, η', calculated as

$$\eta' = \frac{C_T J_a}{C_P}. \tag{8}$$

Similar to equation (7), the moments M_x and M_y are non-dimensionalised using the following expressions:

$$C_{M_x} = \frac{M_x \Omega}{\rho n^3 D^5} \tag{9}$$

$$C_{M_y} = \frac{M_y \Omega}{\rho n^3 D^5}. \tag{10}$$

These coefficients will be used for evaluation of the experimental results and development of analytical models.

2.7 Uncertainty analysis

The uncertainty of the load measurements has been evaluated using an APC propeller with 11 inch diameter and 7 inch/revolution pitch. Three independent tests were carried out by reassembling the system and carrying out the measurements at wind tunnel speeds of $V_\infty = 0$, 5, 10 and 15 m/s ($J = 0$, 0.22, 0.44, 0.65), a constant rotational speed of 6000 RPM. The results showed that the maximum standard deviation in thrust, torque, x-moment and y-moment to be 0.31 N, 0.008 Nm, 0.017 Nm and 0.005 Nm, respectively. The estimated load and torque uncertainty is used along with the uncertainty of the angular speed of the propeller (measured by the electronic speed controller), and the air temperature (measured by the thermocouples in the wind tunnel), to estimate the uncertainty of C_T, C_P, and C_M coefficients. The error propagation analysis demonstrated that the maximum relative uncertainty at $V_\infty = 15$ m/s ($J = 65$) is 6% and 4% for C_T and C_P, respectively. The uncertainties for the moment coefficients C_{Mx} and C_{My} are particularly high at $\alpha_P = 0°$, reaching 39% uncertainty due to the negligible moments at this angle of attack. However, the uncertainty reduces to below 8% for $\alpha_P > 10°$ as the measured moments become larger.

3   Experimental Results

3.1 Thrust generation

The coefficient of thrust is presented for the two SF propeller models with 4.7 in/rev and 6 in/rev pitch, and the SP model with 5 in/rev and 6 in/rev pitch in Fig. 4 (a), (b), (c), and (d) as a function of J and J_a, respectively. The angle-of-attack of the propeller disk is varied within $0° \leq \alpha_P \leq 90°$. The results of the SF propellers in Fig. 4(a) and (b) show that for the tests conducted at $\alpha_P \leq 60°$, the value of C_T reduces with increases in J. At $\alpha_P \geq 70°$, C_T is constant or increases slightly with increasing J for the SF propellers. There is a small increase of C_T with J at $\alpha_P = 90°$, which was also observed by Carrol [7]. The C_T-J data also shows a common trend that an increase of α_P results in higher coefficients of thrust, for any particular value of J. This behavior agrees with that found by Kuhn and Draper [2] and McLemore and Cannon [3], in which the value of C_T increases with increasing α_P at a constant J. The results obtained by Carrol [7] demonstrated a larger rate of increase of C_T (at a constant J) when α_P was increased. The behavior of the SP model propellers in Fig. 4(c) and (d) is similar to the SF models. Both SP12×5 and SP12×6 propellers exhibit reduction of C_T with an increase of J for $\alpha_P < 60°$. It is also observed that, for small free-stream advance ratio of $J < 0.2$, the C_T-J curves for different α_P approximately overlap, suggesting that the influence of α_P on the thrust generation of the SP propellers is not significant in this regime.
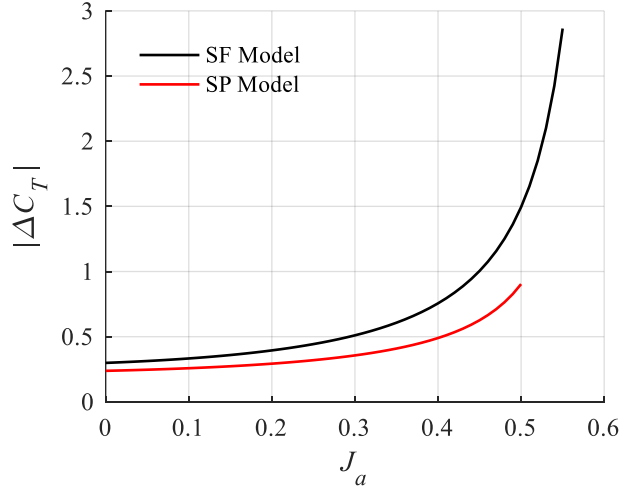
The use of the inflow advance ratio, J_a, results in the overlap of C_T data for different values of α_P into one common trend for each propeller. For a constant, Ω, higher values of α_P translate to lower values of J_a. Therefore, in Fig. 4 (a) to (d), the C_T data points contract into a smaller range of J_a with increase of α_P. This is true for all values of α_P except for two cases at $\alpha_P = 0°$ and $90°$. At $\alpha_P = 0°$, the C_T-J_a curves are identical to the C_T-J plots, since for $\alpha_P = 0°$, J and J_a are identical. The second case corresponds to $\alpha_P = 90°$, which represents a complete edgewise flow. Hence no portion of the free stream flows in the direction of the thrust vector, resulting in a constant value of $J_a = 0$ for all tests performed at this α_P. In addition to the experimental data, the plots in Fig. 4 include a second-order fit of C_T-J_a data and the corresponding equation. This second-order fit can be used to estimate the thrust of the four propellers at a variety of α_P and free-stream conditions.
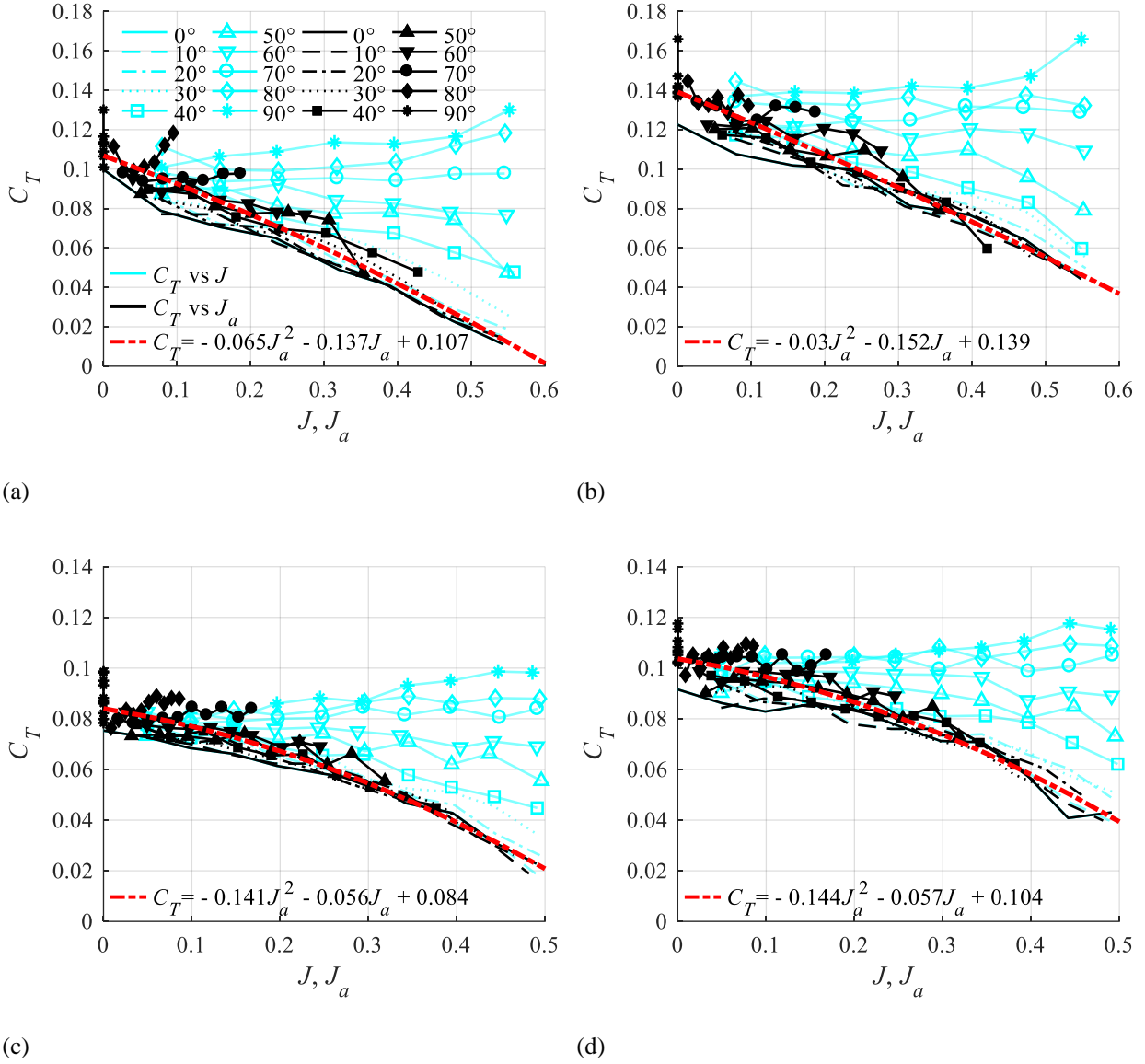
Fig. 4 C_T as a function of J and J_a for multiple values of α_P, for (a) SF12×4.7, (b) SF12×6, (c) SP12×5, and (d) SP12×6 propellers.

For both the SF and SP models, an increase in the propeller pitch results in larger C_T. This trend is observed by comparison of Fig. 4(a) with (b) for the SF when the propeller pitch increases from 4.7 to 5 in/rad, and also by comparison of Fig. 4(c) with (d) when the propeller pitch increases from 5 to 6 in/rad for the SP propeller. The absolute thrust variation through an increase of the propeller pitch from 4.7 to 5 in/rad and from 5 to 6 in/rad for the SF and the SP propellers versus J_a is estimated by subtracting the second-order fits of Fig. 4. The results are plotted in Fig. 5, for

14

both propeller models, showing that the thrust gain increases exponentially with increasing J_a. Therefore, a propeller with larger pitch produces a larger thrust coefficient at larger J_a (i.e., smaller α_P) and for operations at large α_P a large propeller pitch is not required.


Fig. 5 Variation in C_T as a result of increase in the nominal pitch of the propeller versus the inflow advance ratio J_a, for the SF and SP models. The ΔC_T of the SF and the SP are calculated as [$C_{T,\ SF12\times4.7}$ - $C_{T,\ SF12\times6}$] and [$C_{T,\ SP12\times5}$ - $C_{T,\ SP12\times6}$], respectively.

3.2 Power consumption

The plots in Fig. 6 (a)-(d) show the variation of C_P as a function of J and J_a for $0° \leq \alpha_P \leq 90°$ for the four propellers investigated. For $J < 0.3$, there are marginal differences in the power consumption of the two SF propellers for various values of α_P in Fig. 6 (a) and (b). However, for $J > 0.3$, the tests at different α_P start to depart from each other, and a difference becomes evident. In the range of $J > 0.3$, for both SF propellers, C_P demonstrates a decreasing trend for $\alpha_P < 50°$, and for $\alpha_P > 50°$ an increasing trend with increase of J. This response was also observed by Carroll [7], where a decreasing trend was seen for $\alpha_P < 50°$ and $J < 0.4$. The plot in Fig. 6(b) shows that for the SF12×6 propeller tests at $\alpha_P = 90°$, the slope of the power consumption curve increases with J. The variation of C_P is also small for the SP12×5 and SP12×6 propellers in Fig. 6 (c) and (d) for a different α_P. For both SP models, the C_P-J lines for multiple α_P overlap for the range of $J < 0.4$. Similar to the results for thrust, the plots of C_P-J_a for different α_P overlap. Fig. 6 also includes a second order polynomial fit over the C_P-J_a data for power prediction. The decrease of C_P with respect to J observed for the C_P-J curves at $\alpha_P = 0°$ is in agreement with the findings by Brandt and Selig [1] for SP and SF propellers of similar size (11 inch diameter) tested at the same J range.

15
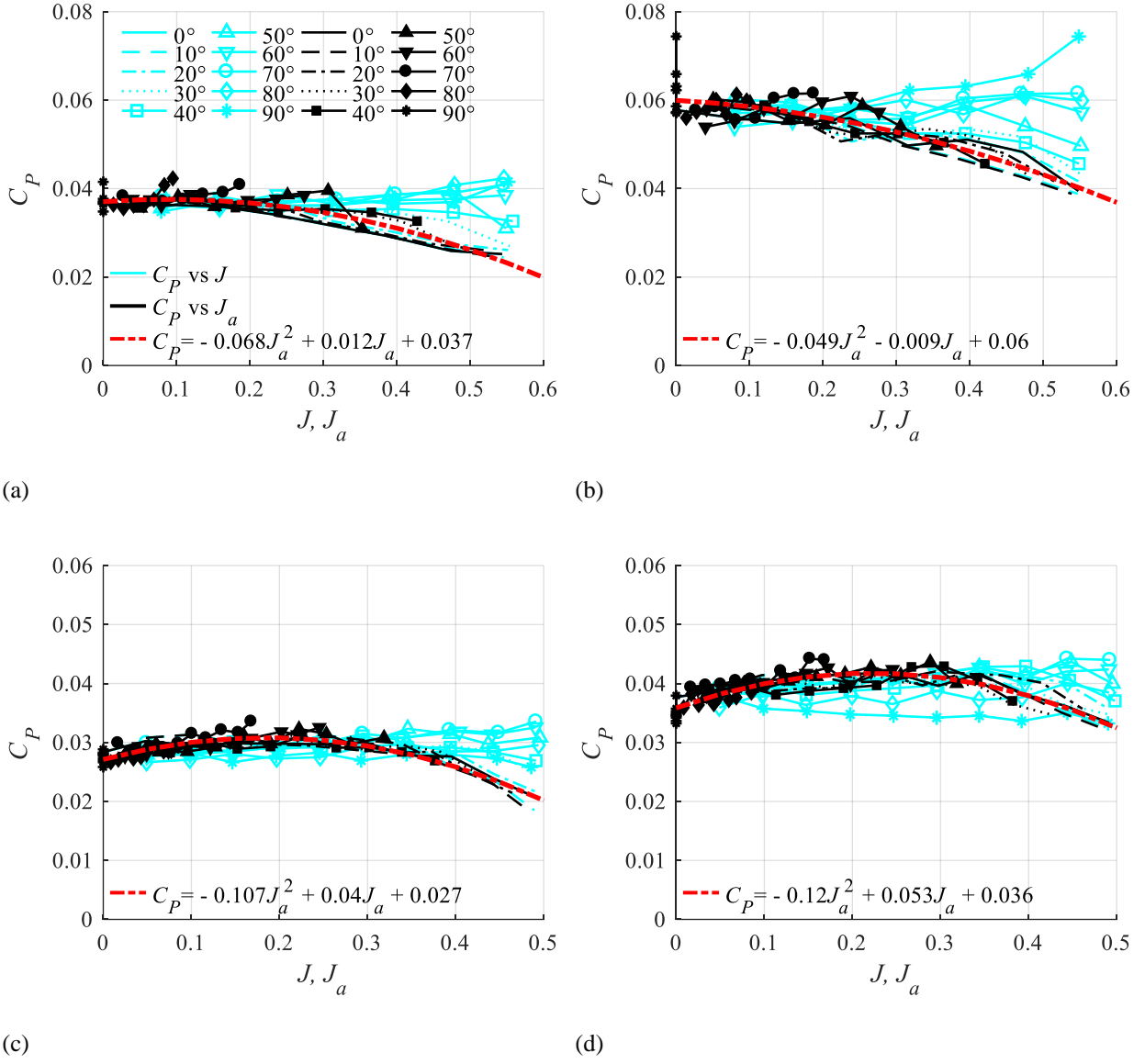
Fig. 6 C_P as a function of J and J_a for multiple values of α_P, for (a) SF12×4.7, (b) SF12×6, (c) SP12×5, and (d) SP12×6 propellers.

The C_P-J_a curves in Fig. 6 (a) to (d) demonstrate a parabolic variation of C_P for all the propellers tested. The parabolic response of the C_P-J_a curves was also observed by McLemore and Cannon [3]. The maximum C_P values obtained were 0.042, 0.074, 0.034 and 0.044 at J_a = 0.095, 0, 0.17 and 0.15 for the SF12×4.7, SF12×6, SP12×5 and SP12×6 propellers, respectively. It is also evident that an increase in C_P is obtained by increasing the nominal pitch

16

of the propellers. The percentage of increase in C_P obtained from an increase in nominal pitch from 4.7 to 6 inches/rev

for the SF propellers, and from 5 to 6 inches/rev for the SP propellers is shown in Fig. 7. It can be seen that the

increment is parabolic with respect to J_a, with the minimum value at J_a=0.25 and $J_a = 0$ for the SF and SP models,

respectively.
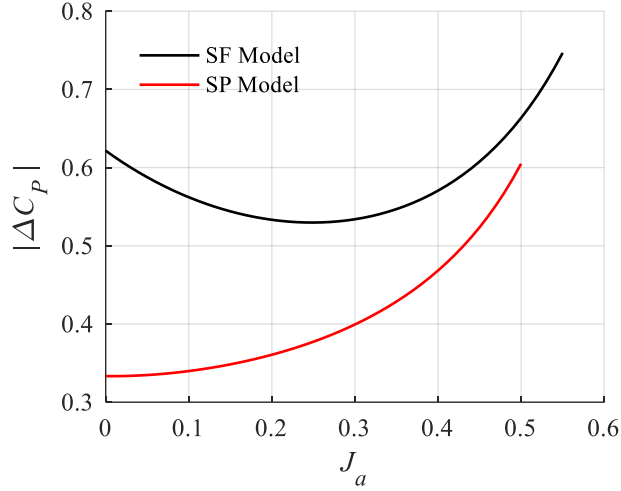

Fig. 7 Variation in C_P as a result of increase in the nominal pitch of the propeller versus the inflow advance ratio J_a, for the SF and SP models. The ΔC_P of the SF and the SP are calculated as [$C_{P, \text{SF}12\times4.7}$ - $C_{P, \text{SF}12\times6}$] and [$C_{P, \text{SP}12\times5}$ - $C_{P, \text{SP}12\times6}$], respectively.

3.3 Pitch and yaw moments

The plots presented in Fig. 8 (a) to (d) show variation of the pitch moment C_{My} as a function of J for the four

propellers tested within $0 \leq \alpha_P \leq 90°$. The results for both the SF and SP propellers in Fig. 8 (a) and (b) demonstrate

that the value of C_{My} increases with increase of J and α_P. Yaggy and Rogallo [4] also obtained the same trend between

C_{My} and α_P in their experiments. For the SF12×4.7 propeller it is observed in Fig. 8(a) that there is a negligible

variations of C_{My} with respect to J at $\alpha_P < 30°$, while for $\alpha_P > 30°$ the rate of change of C_{My} with respect to J is larger.

A variation similar to the variation of C_{My} with J increasing at larger α_P is also observed for the other propeller. The

comparison of Fig. 8 (a) and (b) shows that for the C_{My}-J curves of the SF12×4.7 propeller are closer together than the

curves for the SF12×6 propeller. This suggests that a propeller with larger pitch (and larger C_T) is more susceptible to

variations in C_{My} due to changes in α_P. The results for the SP propeller models in Fig. 8 (c) and (d) show that, when

α_P increases from 40° to 50°, the moment significantly increases. This suggests two regimes for C_{My} variation with

respect to α_p: a region where C_{My} is invariant with respect to J at the approximate range of $\alpha_P < 40°$; and a region of

increasing C_{My} with respect to J at the approximate range of $\alpha_P > 50°$.


(a)

(b)

(c)

(d)
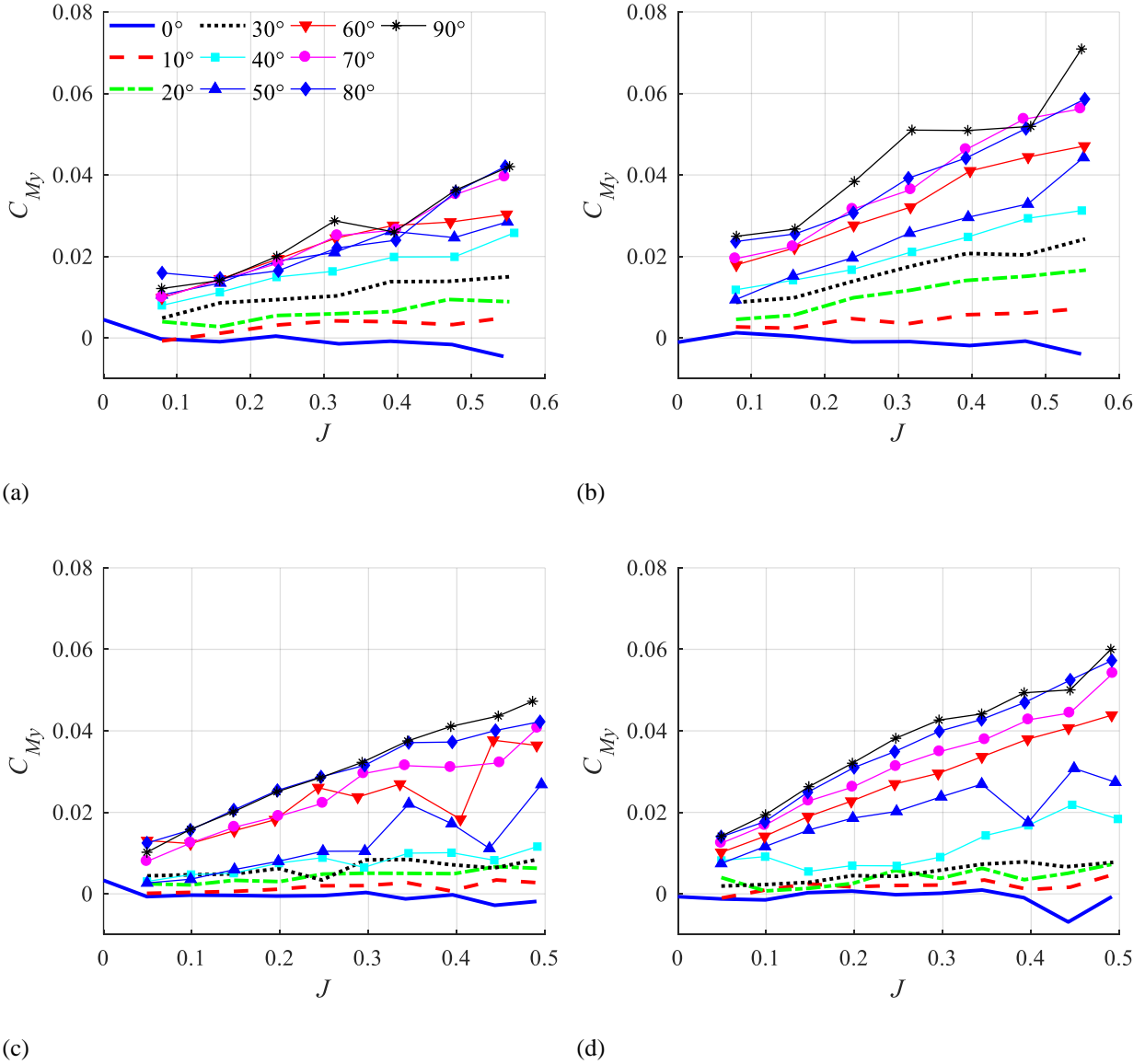
Fig. 8 The variation of C_{My} as a function of J for multiple values of α_P for (a) SF12×4.7, (b) SF12×6, (c) SP12×5, and (d) SP12×6 propellers.

The coefficient of yaw moment about the x-axis, C_{Mx}, is shown in Fig. 9 (a) to (d) as a function of J, for the

SF12×4.7, SF12×6, SP12×5 and SP12×6 propellers, respectively. It must be noted that in the results presented in Fig.

9 (a) to (d), the value of C_{Mx} includes the moment generated by the drag of the motor casing acting at a distance from

the load cell. The operation of the propeller results in a negative x moment, which increases with increases of J and α_P. A larger increase of C_{Mx} for the SP12×6 propeller is observed when α_P increases from 50° to 60° in Fig. 9(d). The results from Fig. 8 and Fig. 9 suggest that increasing the angle-of-attack of the rotor disk while maintaining a constant J (or vice versa) increases the asymmetry of thrust distribution over the rotor disk.

3.4 Propulsive efficiency

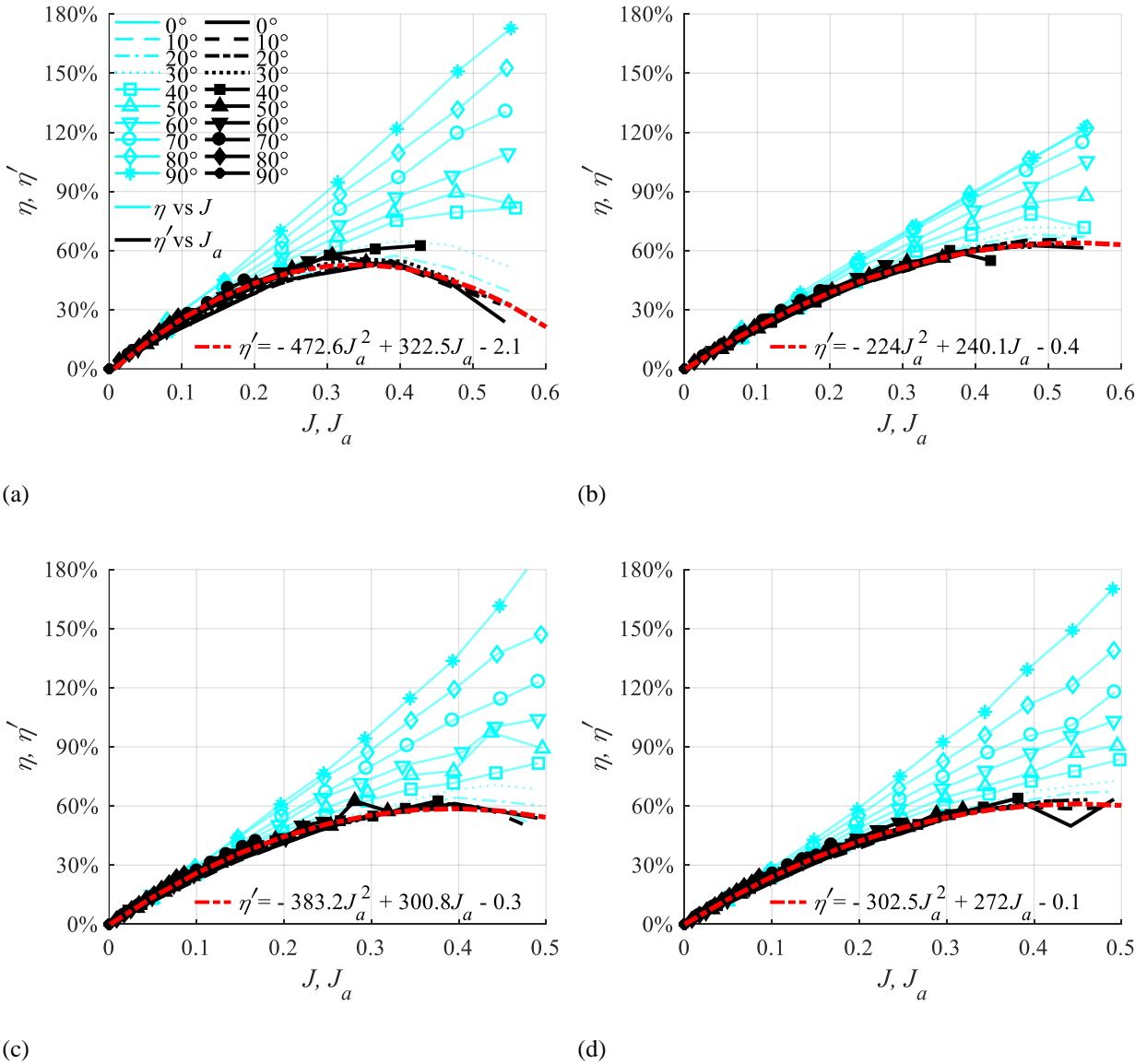The propulsive efficiency of the four propellers is evaluated and shown in Fig. 10 (a) to (d) for $0 \leq \alpha_P \leq 90°$. The efficiency is obtained using equations (5) and (8) in terms of η and η' is plotted as η-J and η'-J_a curves. For $\alpha_P < 40°$ of Fig. 10(a), the η-J curves has a local maximum at about $J \sim 0.4$. In Fig.10 (b) to (d), for $\alpha_P < 40°$ the local maximum is absent; an increase of η with J is observed with the maximum efficiency occurring at the largest J value. The tests conducted at $\alpha_P > 40°$ in Fig. 10(a) to (d) show a linear increase of η with J. It is also observed that SF12×6 is less efficient than the SF12×4.7 propeller for $\alpha_P > 60°$. Fig. 10 also demonstrates that the efficiency of the propeller increases with increasing α_P for all J values. At high J and high α_P, all four propellers exhibit an η value greater than 100%. This is associated with the J parameter in the definition of η in equation (5). It is important to note that the wind tunnel velocity, rather than the actual airspeed of the vehicle, sets J value. Therefore, it is possible to obtain η values larger than one.

19
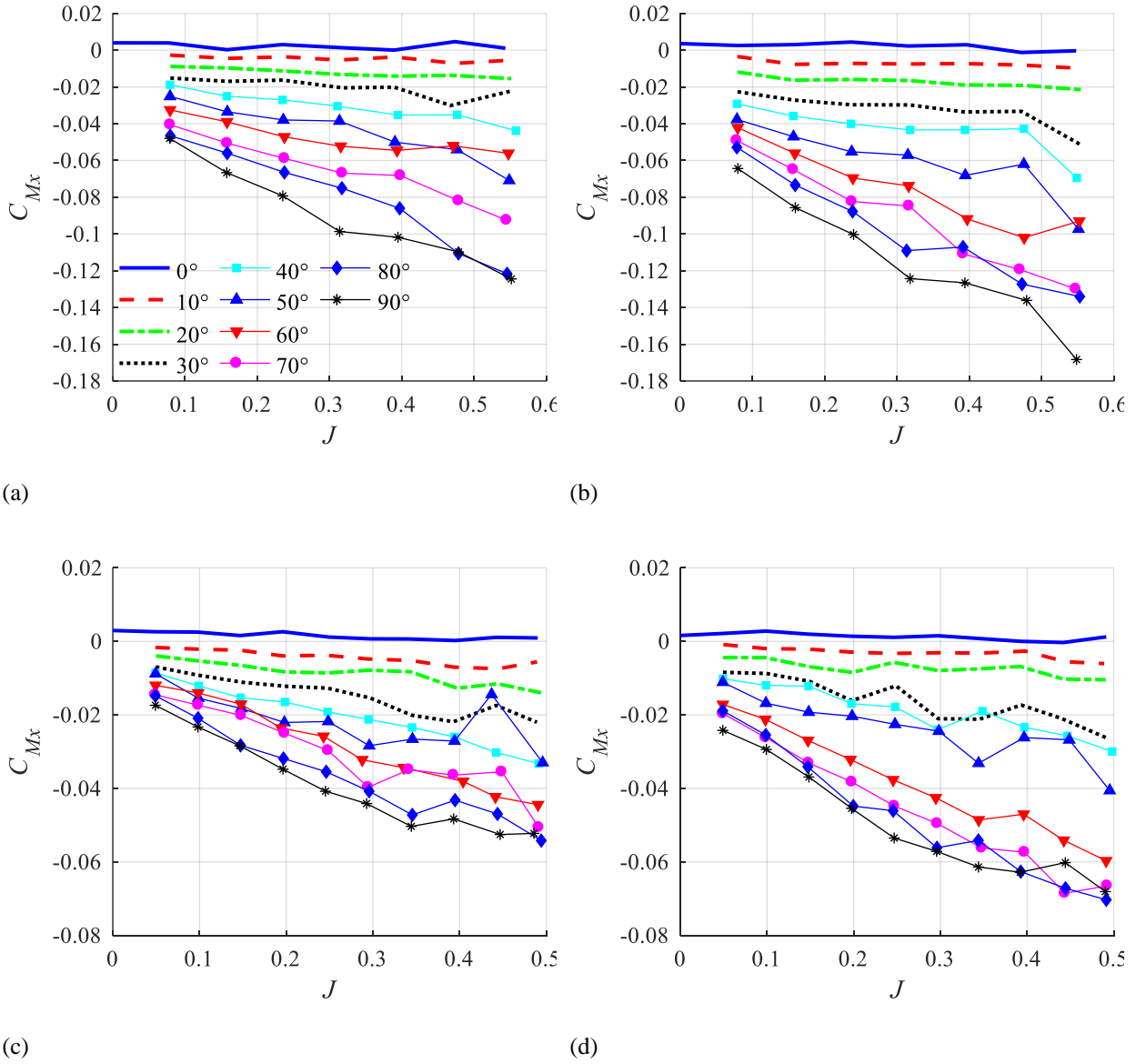
Fig. 9 The variation of C_{Mx} as a function of J, for multiple values of α_P, for propellers (a) SF12×4.7 (b) SF12×6 (c) SP12×5 (d) SP12×6

For a propeller in a multi-rotor vehicle, in which the rotor disk plane is tilted with respect to the free-stream, the definition of propulsive efficiency may be measured with regard to more than the forward advancing speed of the vehicle; it should be measured using the velocity component that is collinear with the direction of the thrust vector. Therefore, η'-J_a curves have been presented as well. The η'-J_a curves in Fig. 10 (a) to (d) for all four propellers demonstrate significant overlap for all α_P values. For both the SF and SP model propellers, the higher pitch propeller

(SF12×6 and SP12×6) achieves its maximum value of η' at a higher value of J_a than does the low pitch model. The fit of the second-order polynomials are developed over the η'-J_a efficiency curves for each propeller and shown in Fig. 10 (a) to (d). The percentage difference in η' due to a change in the nominal pitch of the propellers was calculated using the polynomial models, and the results are shown in Fig. 11. It can be observed from Fig. 11 that an increase in the nominal pitch of the propeller depends on J_a. It is also noted from Fig. 11 that the J_a value at which the higher pitch propeller begins to improve η' occurs at approximately J_a=0.3, for both propeller models.

Fig. 10   Modified propulsive efficiency as a function of the modified advance ratio, for multiple values of α_P, for propellers (a) SF12×4.7 (b) SF12×6 (c) SP12×5 (d) SP12×6

21
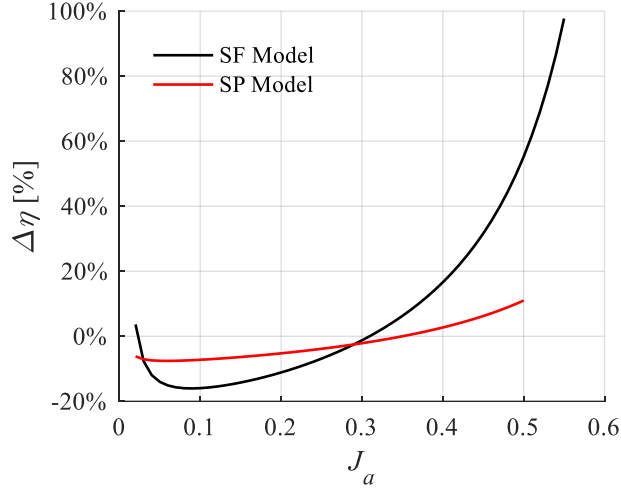
Fig. 11   **Variation in η' as a result of increase in the nominal pitch of the propeller versus the inflow advance ratio J_a, for the SF and SP models. The $\Delta\eta'$ of the SF and the SP are calculated as [$\eta'_{SF12\times4.7}$ - $\eta'_{SF12\times6}$] and [$\eta'_{SP12\times5}$ - $\eta'_{SP12\times6}$], respectively.**

4   Analytical Modeling

4.1 Sectional lift and drag coefficients

In order to interpret the experimental results, an analytical model of the performance of the propeller at a non-zero

angle-of-attack is developed. The analytical model is based on the blade element theory (BET) applied to the forward

flight of a helicopter rotor, adapted from Leishman [13]. The blade element theory indicates that differential lift, *dL*,

and drag, *dD*, generated by each blade element (shown in Fig. 12(a)) depends on the inflow angle, φ. The inflow angle,

φ, is the angle between resultant velocity vector incident on the blade element (V_R) and the rotor disk as shown in Fig.

12(b). Therefore, the differential thrust, *dT*, is

$$dT = dL \cdot \cos(\varphi) - dD \cdot \sin(\varphi), \tag{11}$$
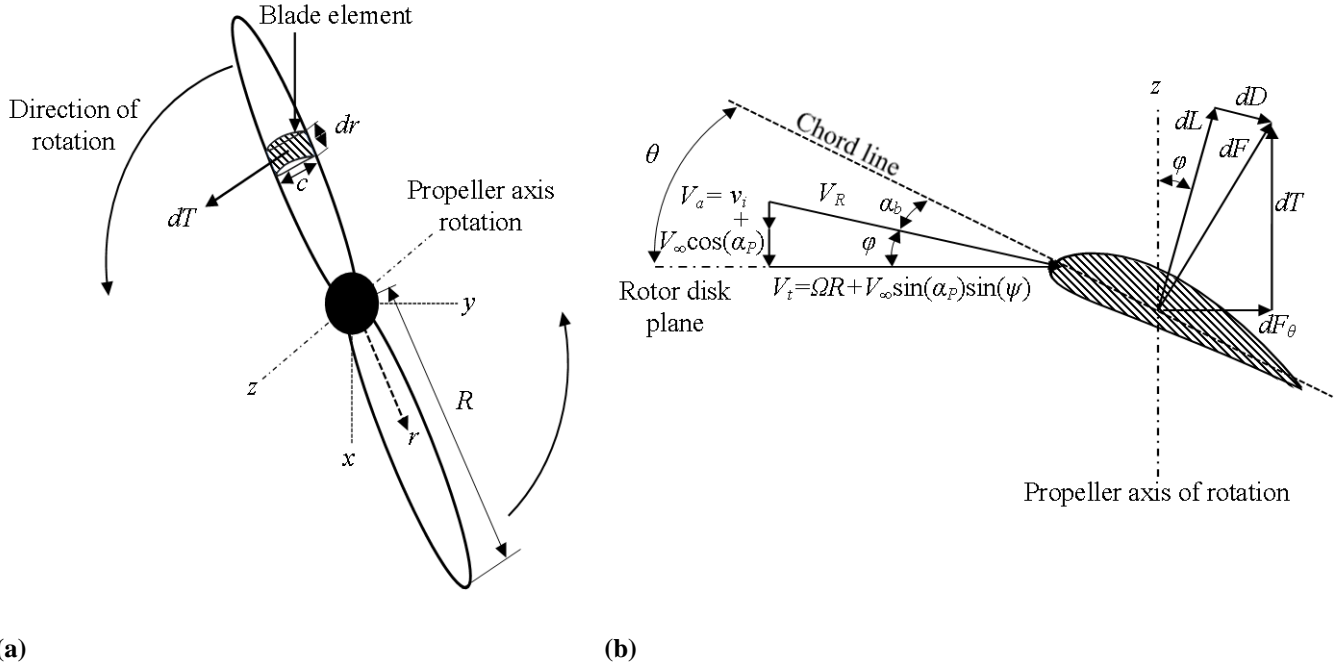
where the differential lift is defined as,

$$dL = \frac{1}{2}\rho V_R^2 C_l c \cdot dr, \tag{12}$$

and the differential drag as

$$dD = \frac{1}{2}\rho V_R^2 C_d c \cdot dr, \tag{13}$$

22

where C_l and C_d are the lift and drag coefficients of the airfoil, respectively. The chord length distribution over the blade is calculated using the fourth order polynomial equation obtained from Fig. 2(b).

(a)   **(b)**

Fig. 12   (a) Diagram defining the blade element within the propeller. (b) The velocity vector diagram that is incident to the blade element. The diagram also includes the differential forces acting upon the blade element.

The sectional lift and drag coefficients used in Equations (12) and (13), for the NACA 4412 and Eppler 63 airfoils, were obtained from the open source XFOIL software. Values for C_l and C_d were obtained for $-10° < \alpha_P < 40°$, and for Re numbers: $1\times10^3 - 5\times10^3$ every 1×10^3, $10\times10^3 - 100\times10^3$ every 10×10^3, and $100\times10^3 - 160\times10^3$ every 20×10^3. With this C_l and C_d data, eighteen fourth-order polynomials of these coefficients as a function of α_b were obtained to calculate C_l and C_d for any α_b within the range $-10° < \alpha_P < 40°$. For the α_P values at $\alpha_P < -10°$ or $\alpha_P > 40°$, the C_l and C_d corresponding to the α_P extrema (i.e., $\alpha_P = -10°$ or $40°$) were used. The Re distribution over the rotor disk is shown in Fig. 13 for $\alpha_P = 90°$, approximated using the geometrical information from Fig. 2 (b), the rotational speed of the experiments, and the maximum free-stream velocity for the SF and SP models as

$$Re = \frac{\rho V_R c}{\mu},$$

$$(14)$$

where μ is the dynamic viscosity of air. The $\alpha_P = 90°$ condition is displayed because it is the condition where the propeller's cross-section experiences a maximum Re of 160,000 and 180,000 for the SF and SP propellers,

23

respectively. For $\alpha_b < -10°$ and $\alpha_b > 18°$, $C_l = 0$, was prescribed. In regards to C_d, the extrema values of C_d in the C_d-α_b curves were prescribed for $\alpha_b < -10°$ and $\alpha_b > 18°$. For more accurate estimations of C_l and C_d, a study such as the one performed by Critzos [14], where the aerodynamic performance of a NACA 0012 airfoil was dynamically measured within $0°<\alpha_b<180°$ is necessary.

(a)   (b)
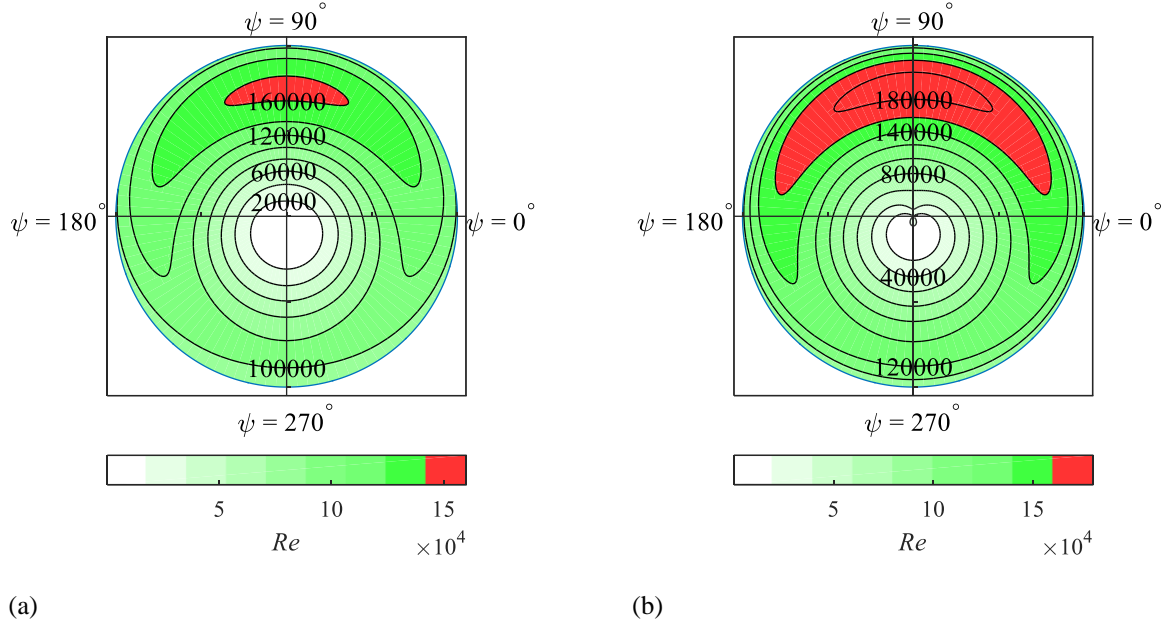
Fig. 13   Distribution of *Re* over the rotor disk, for the (a) SF12×6 and (b) SP12×6 propellers at $\alpha_P = 90°$ and V_∞=14 m/s and 20 m/s, respectively.

The rotor disk was discretized using 100 radial elements, over 100 azimuthal locations (angularly separated by $2\pi/100$ rad). The location of any blade element in the rotor disk may be described using the Cartesian coordinate system as defined in Fig. 3(c), with coordinates x and y being the lateral and longitudinal directions, respectively, and where the origin is located at the propeller hub. In other words, it is a polar coordinate system, where the radial coordinate r represents the distance from the hub, and the azimuthal angle ψ is the angular location in degrees. The area in the rotor disk occupied by the hub has been treated as a flat disk.

4.2 Local effective angle-of-attack

As shown in Fig. 12(b), the effective angle-of-attack of a blade element, α_b, is defined as the angle formed between the relative wind vector, V_R, and the chord line. For a rotor operating at a non-zero α_P and constant Ω, the free stream velocity can be decomposed into an axial and a tangential component relative to the rotor disk, as shown in Fig. 3(c).

The resultant velocity incident on the blade elements, V_R, can also be decomposed into a component that is perpendicular to the rotor disk (V_a) and one that is tangential to the rotor disk (V_t), as shown in Fig. 12(b). These components are functions of the following: V_∞; α_P; the induced axial velocity, v_i; the distance, r, of the blade element from the center of the rotor; and the azimuthal location of the blade element in the rotor disk, ψ, such that

$$V_a = V_\infty \cos(\alpha_P) + v_i, \tag{15}$$

and

$$V_t = \Omega r + V_\infty \sin(\alpha_P) \sin(\psi). \tag{16}$$

Equations (15) and (16) are simplified versions of the helicopter rotor performance equations presented by Leishman [13] for forward flight since the effects of blade flapping and blade flapping displacement (coning) are neglected due to the propellers' small diameters. Using equations (15) and (16), α_b is computed as the difference between the pitch angle of the blade element and the inflow angle as follows:

$$\alpha_b = \theta - \varphi, \tag{17}$$

where the inflow angle can be calculated using the following expression:

$$\varphi = \text{atan}\left(\frac{V_a}{V_t}\right) = \text{atan}\left(\frac{V_\infty \cos(\alpha_P) + v_i}{\Omega r + V_\infty \sin(\alpha_P) \sin(\psi)}\right). \tag{18}$$

The pitch angle at a particular radial location, r, is calculated using the fourth order polynomial equation obtained from Fig. 2(a).

4.3 Induced velocity calculation

Previously, the non-uniform distribution of the induced velocity, v_i, over the rotor disk area during forward flight of a helicopter has been modeled through the use of "inflow models". These models have been developed and evaluated mostly for rotor angle-of-attack of approximately $75° \leq \alpha_P < 90°$, which corresponds to the forward flight of a helicopter. The non-dimensional induced inflow, λ_i, is defined as

$$\lambda_i = \frac{v_i}{\Omega R}. \tag{19}$$

An early model developed by Glauert [15] implements a longitudinal distribution of λ_i across the rotor disk area, through a weighing factor, k_x, such that

$$\lambda_i = \lambda_0 \left(1 + k_x \frac{x_l}{R}\right), \tag{20}$$

where λ_0 is the induced inflow ratio in forward flight, as derived by the momentum theory. This parameter is numerically obtained by solving

25

$$\lambda_0 = \frac{v_i}{\Omega R} = J_t \cot(\alpha_P) + \frac{C_{T,h}}{2\sqrt{J_t^2 + \lambda_0^2}}. \tag{21}$$

In this equation J_t is the tangential advance ratio, based on the component of the free stream velocity that flows tangentially to the rotor disk, defined as

$$J_t = \frac{V_\infty \sin(\alpha_P)}{\Omega R}. \tag{22}$$

It must be noted that in equation (22), the value of J_t is calculated using the blade tip speed, complying with the American format used by Leishman [13]. A simple, fixed-point iteration algorithm in MATLAB was used to numerically solve for λ_0 in equation (21) with a residual error of 0.05%. A modification of Glauert's model includes an additional variation in the lateral direction (*y* axis), as presented by Leishman [13], which is expressed as

$$\lambda_i = \lambda_0 \left(1 + k_x \frac{x_l}{R} + k_y \frac{y_l}{R}\right) = \lambda_0 \left(1 + k_x \, r \cos(\psi) + k_y r \sin(\psi)\right). \tag{23}$$

Glauert [15] suggested k_x=1.2 and k_y=0 as the values for the weighing factors. Other studies, such as the ones performed by Coleman *et al.* [16], Drees [17], and Pitt and Peters [18], suggest methods of calculating the weighing coefficients, k_x, and, k_y, as functions of the wake skew angle, χ, which is the angle between the axis of the ideal helical streamtube of the wake and the rotor's axis of rotation, calculated as

$$\chi = \tan^{-1}\left(\frac{J_t}{J_a' + \lambda_i}\right). \tag{24}$$

Here J_a' is the inflow advance ratio, based on the component of the free-stream velocity that flows perpendicular to the rotor disk, and it is non-dimensionalised by the tip speed as

$$J_a' = \frac{V_\infty \cos(\alpha_P)}{\Omega R}. \tag{25}$$

Coleman *et al.* [16] characterized the longitudinal distribution of the induced velocity using vortex, in which the weighting factor is a function of χ, thus, becoming the first attempt to analytically calculate the weighting coefficients proposed by Glauert [15]. Using a modification of the wake geometry defined by Coleman *et al.* [16], Drees [17] developed a model that aimed to include the azimuthal changes in the bound circulation of the blade elements. To account for forward flight conditions, Pitt and Peters [18] modified a model previously developed for hovering flight. Chen [19] claims that Pitt and Peters' model performs relatively well in comparison with the other models mentioned above. These models are first harmonic models, and their analyses are based on the assumption of a time-averaged behavior of the rotor disk. Chen [19] provides comparisons of the Drees'[17] model and the Pitt and Peters [18] model with experimental data from a wind tunnel investigation of the downwash of a helicopter by Cheeseman and Haddow

[20]. The tests were performed at $\alpha_P \approx 88.25°$ and the rotor radius was 0.675 m. They report that the Drees [17] model deviates from the experimental data by 10% to 16%, while the Pitt and Peters [18] model by 2% to 7%, depending on the operating condition. The k_x and k_y coefficients of these methods, based on the wake skew angle, are summarized in Table 2, and will be used for comparison in this section. In the case of Drees [17], at $\alpha_P = 0°$ a value of $k_x = 0$ is prescribed. An intensive summary of the inflow models used can be found in a literature survey compiled by Chen [19].

Table 2: The weighing coefficients for the linear distribution of the induced inflow.

Author(s)	k_x	k_y
Coleman *et al.* [16]	$\tan(\chi/2)$	0
Drees [17]	$(4/3)(1-\cos(\chi)-1.8J_t^2)/\sin(\chi)$	$-2J_t$
Pitt and Peters [18]	$(15\pi/23)\tan(\chi/2)$	0

4.4 Tip loss factor

An estimation of the effects of tip loss based on the approximation formulated by Prandtl [21] was applied to the analytical results from Glauert [15], Coleman et. al. [16] Drees [17] and Pitt and Peters [18]. The idea behind the formulation from Prandtl [21] is that the tip losses can be accounted for using a factor which reduces the effective rotor disk area of the propeller. Prandtl [21] suggested that an effective blade radius, R_{eff}, may be calculated as

$$\frac{R_{eff}}{R} = 1 - \left(\frac{1.386}{N}\right) \cdot \frac{\lambda_i}{\sqrt{1+\lambda_i^2}}. \tag{26}$$

5   Comparison to Existing Analytical Models

The analytical models described in the previous sections were implemented to the SP12X6 propeller and compared with the experiments at $V_\infty = 8, 10, 12$ and 14 m/s ($J = 0.197, 0.246, 0.295$, and 0.344) in Fig. 14 (a) to (d), respectively.

5.1 Evaluation of existing inflow models

The results show that the models suggested by Glauert [15] and Coleman *et al.* [16] provide the closest approximations to the experimental data. For $\alpha_P > 0°$ the models by Glauert [15] and Coleman *et al.* [16] achieve

27

discrepancies lower than 15%. The models by Dress [17] and Pitt and Peters [18] achieve values close to each other, but over-estimate the thrust obtained from the experiments. These two models have a maximum discrepancy with respect to the experimental data of about 30%, both at V_∞= 8 m/s ($J = 0.197$) and α_P=0°. For $\alpha_P > 0°$ the models of Dress [17] and Pitt and Peters [18] show discrepancies lower than 33% with respect to the experimental data. The BET model with uniform inflow provides an over-estimation of the thrust force generated at all values of α_P, with the exception of the axial flow (α_P=0°), where it has a maximum discrepancy with respect to the experimental data of 36.75% at V_∞= 14 m/s ($J = 0.344$), and for $\alpha_P > 0°$ it has a maximum discrepancy of 22%. However, the models can predict the overall trend of thrust generation as a function of α_P. The closest approximation to the experimental data is achieved by the model from Glauert [15]. Even at the range $75° \leq \alpha_P \leq 90°$, where they are most commonly applied for forward flight of a helicopter, the results exhibit discrepancies between the inflow models presented and the experimental data. In an investigation on the induced velocity produced by a 0.675 m rotor operating at $J_a = 0.067$ and 0.1, Cheeseman and Haddow [20] used hot wire anemometry data to experimentally determine χ and calculate k_x using Coleman's method. They compared the results with the estimated χ from equation (24) and observed that the deviation in these results was about 45% to 56%. The difference between the models and the experimental results is mainly associated with the smaller Re number of the current propeller relative to the Re number of full-scale helicopters, used for developing the models.
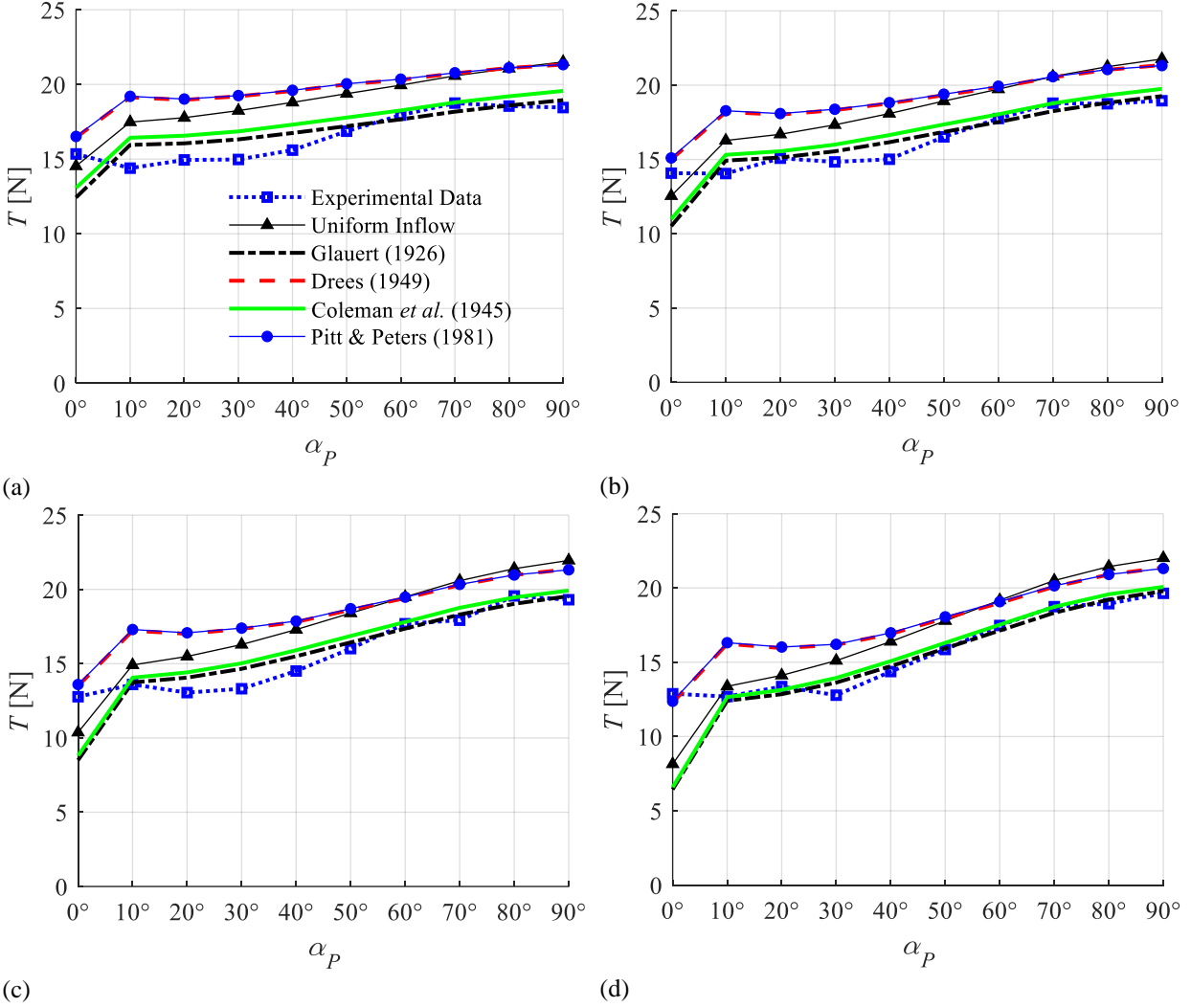
Fig. 14 Comparison between analytical and experimental thrust data, for *J* values of (a) 0.197 (b) 0.246 (c) 0.295 and (d) 0.345.

5.2 Distribution of α_b and thrust over the propeller disk

Out of the induced velocity models presented in section 4, the model by Drees [17] is the only one that calculates variations in the induced velocity along the longitudinal and lateral directions within the rotor disk. Therefore, this model has been selected to provide a visual representation of the distribution of α_b and the differential thrust, *dT*, over the rotor disk. The results are presented in Fig. 15 (a) to (h) for $V_\infty = 10$ m/s, $n = 8,000$ RPM ($J = 0.25$), and $\alpha_b = 0°$, 30°, 60° and 90°. The rotor disk plots on the left column of Fig. 15 show the α_b distribution, and the right column shows the distribution of *dT*. As the rotor disk angle (α_p) is increased, α_b increases over the majority of the rotor disk area. The largest α_b is generated by the advancing blades located in the azimuthal coordinates of $0°<\psi<180°$. The

value of α_b inside this region increases in magnitude with increase of α_p achieving a maximum value of $\alpha_b = 20°$. The region of highest α_b shifts towards $90° < \psi < 180°$ as α_p approaches $90°$. It must be noted that in this region the advancing blades achieve α_b values beyond the stall angle of the NACA 4412 airfoil, thus as shown in Fig. 15 (b), (d), (f) and (h) the sections of highest α_b do not necessarily translate to regions of high dT.

(a)
(b)
$\alpha_p = 0°$
(c)
(d)
$\alpha_p = 30°$
(e)
(f)
$\alpha_p = 60°$

30
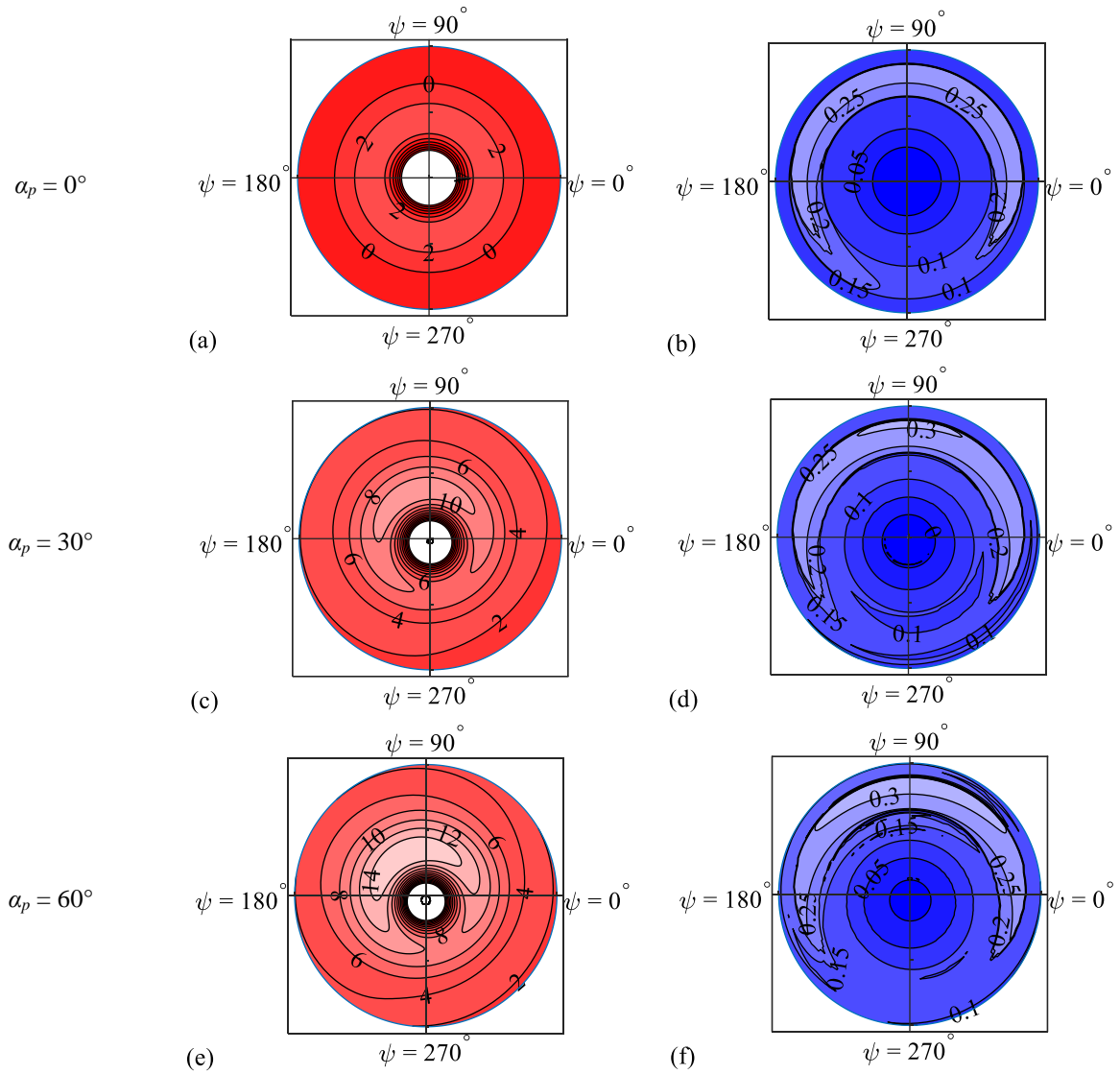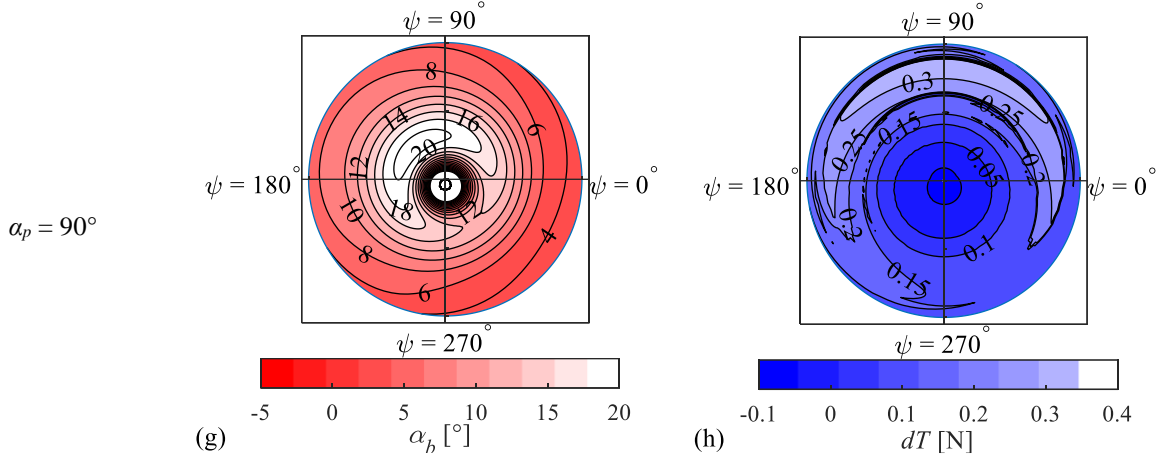
Fig. 15 Analytical estimation of α_b and dT for $V_\infty = 10$ m/s at (a, b) $\alpha_P=0°$, (c, d) $\alpha_P=30°$, (e, f) $\alpha_P=60°$, and (g, h) $\alpha_P=90°$.

6 Conclusion

The aerodynamic performance of four propellers with 12 inch diameter was investigated at propeller angles-of-attack ranging from 0° to 90°. The propeller models tested were two Slow Flyers (SF) with pitches 4.7 in/rev and 6 in/rev, and two Sport (SP) models with pitches of 5 in/rev and 6 in/rev. Wind tunnel tests were executed to a maximum free-stream advance ratio of 0.55 and 0.5 for the SF and SP model propellers, respectively. The wind tunnel data showed that for all four propellers thrust increased with increasing propeller angle-of-attack. Power consumption results demonstrated a lower sensitivity to changes in the propeller angle-of-attack. Due to the difference in performance of the advancing and retreating blades, the moments on the propeller disk increased with increasing propeller angle-of-attack. The results demonstrated that both a pitching and a yawing moment act on the rotor disk when it is subject to a non-zero angle-of-attack. Evaluation of the propulsive efficiency demonstrated that propulsive efficiency of the propeller increases with increases in the propeller angle-of-attack. The analysis also demonstrated that when presented as a function of the inflow advance ratio, the thrust, power, and efficiency curves of the propeller, at different angles-of-attack, overlap.

Previous models in the literature considerably underestimated the thrust of the propeller. The results show that the induced flow model of Glauert [15] and Coleman *et al.* [16] provides the closest approximations to the experimental data. For $\alpha_P > 0°$, these achieve discrepancies lower than 15%. The models by Dress [17] and Pitt and Peters [18] achieve values close to each other, but over-estimate the thrust obtained from the experiments by about 30%. The

31

results showed that the increase of propeller thrust at larger disk angle-of-attack is due to the increase of thrust over the advancing blade. The asymmetry of the thrust distribution over the advancing and retreating blade results in a pitch moment on the rotor disk.

7   Acknowledgements

8   References

[1]   J. B. Brandt and M. S. Selig, "Propeller Performance Data at Low Reynolds Numbers," AIAA Paper 2011-1255, January 2011.

[2]   R. E. Kuhn and J. W. Draper, "Investigation of the Aerodynamic Characteristics of a Model Wing-Propeller Combination and of the Wing and Propeller Separately at Angles of Attack up to 90°," NACA TR-1263, January 1956.

[3]   H. C. McLemore and M. D. Cannon, "Aerodynamic investigation of a four-bladed propeller operating through an angle-of-attack range from 0 to 180 degrees," NACA TN-3228, June 1954.

[4]   P. Yaggy and V. Rogallo, "A Wind-Tunnel Investigation of Three Propellers Through an Angle of Attack from 0 to 85 deg," NACA TN-D-318, May 1960.

[5]   C. E. Hughes and J. A. Gazzaniga, "Low-Speed Wind Tunnel Performance of High-Speed Counterrotation Propellers at Angle-of-Attack," AIAA Paper 89-2583, January 1989.

[6]   J. L. Pereira, "Hover and Wind-Tunnel Testing of Shrouded Rotors for Improved Micro Air Vehicle Design," Ph.D. Dissertation, Aerospace Engineering Dept., University of Maryland, College Park, 2008.

[7]   T. B. Carroll, "A Design Methodology for Rotors of Small Multirotor Vehicles," M.Sc. Disseration, Aerospace Engineering Dept., Ryerson University, Toronto, 2017.

[8]   Drela, M, "QPROP Formulation," MIT Aero & Astro, June 2006.

[9]   S. Goldstein, "On the Vortex Theory of Screw Propellers," *Proceedings of the Royal Society of London. Series A, Containing Papers of a Mathematical and Physical Character*, Royal Society, Vol. 123, London, April 1929, pp 440-465.

[10] B. Theys, G. Dimitriadis, P. Hendrick and J. De Schutter, "Experimental and Numerical Study of Micro-Aerial-Vehicle Propeller Performance in Oblique Flow," *Journal of Aircraft*, Vol. 54, No. 3, 2017, pp. 1076-1084.

[11] M. S. Selig, "Eppler 63 low Reynolds number airfoil," UIUC Airfoil Coordinates Database, http://m-selig.ae.illinois.edu/ads/coord_database.html [retrieved 1 September 2017].

[12] H. Glauert, *The Elements of Aerofoil and Airscrew Theory*, 2nd ed., The Syndics of the Cambridge University Press, London, 1959, Chap. 15.

[13] J. G. Leishman, *Principles of Helicopter Aerodynamics*, 2nd ed., Cambridg University Press, New York, 2006, Chaps. 2-3.

[14] C. C. Critzos, H. H. Heyson and R. W. Boswinkle Jr, "Aerodynamic Characteristics of NACA 0012 Airfoil Section at Angles of Attack from 0 degrees to 180 degrees," NACA-TN-3361, January 1955.

[15] H. Glauert, "A General Theory of the Autogyro," R&M No. 1111, British A.R.C., November 1926.

[16] R. P. Coleman, A. M. Feingold, and C. W. Stempin, "Evaluation of the Induced-Velocity Field of an Idealized Helicopter Rotor," NACA-WR-L-126, June 1945.

[17] J. M. Drees, "A Theory of Airfoil Through Rotors and Its Application to Some Helicopter problems," *Journal of the Helicopter Association of Great Britain*, Vol. 3, No. 2, 1949, pp. 79-104.

[18] D. M. Pitt and D. A. Peters, 'Theoretical Prediction of Dynamic-Inflow Derivatives," *Sixth European Rotorcraft and Powered Lift Aircraft Forum*, Paper No. 47, September 1980.

[19] R. T. N. Chen, "A Survey of Nonuniform Inflow Models for Rotorcraft Flight Dynamics and Control Applications," NASA-TM-102219, November 1989.

[20] I. C. Cheeseman and C. Haddow, "An Experimental Investigation of the Downwash Beneath a Lifting Rotor and Low Advance Ratios," *Fourteenth European Rotorcraft Forum*, Paper No. 8, September 1988.

[21] L. Prandtl, "Applications of Modern Hydrodynamics to Aeronautics," NACA-TR-116, January 1923.